

سورة البقرة الآية: ٣٢

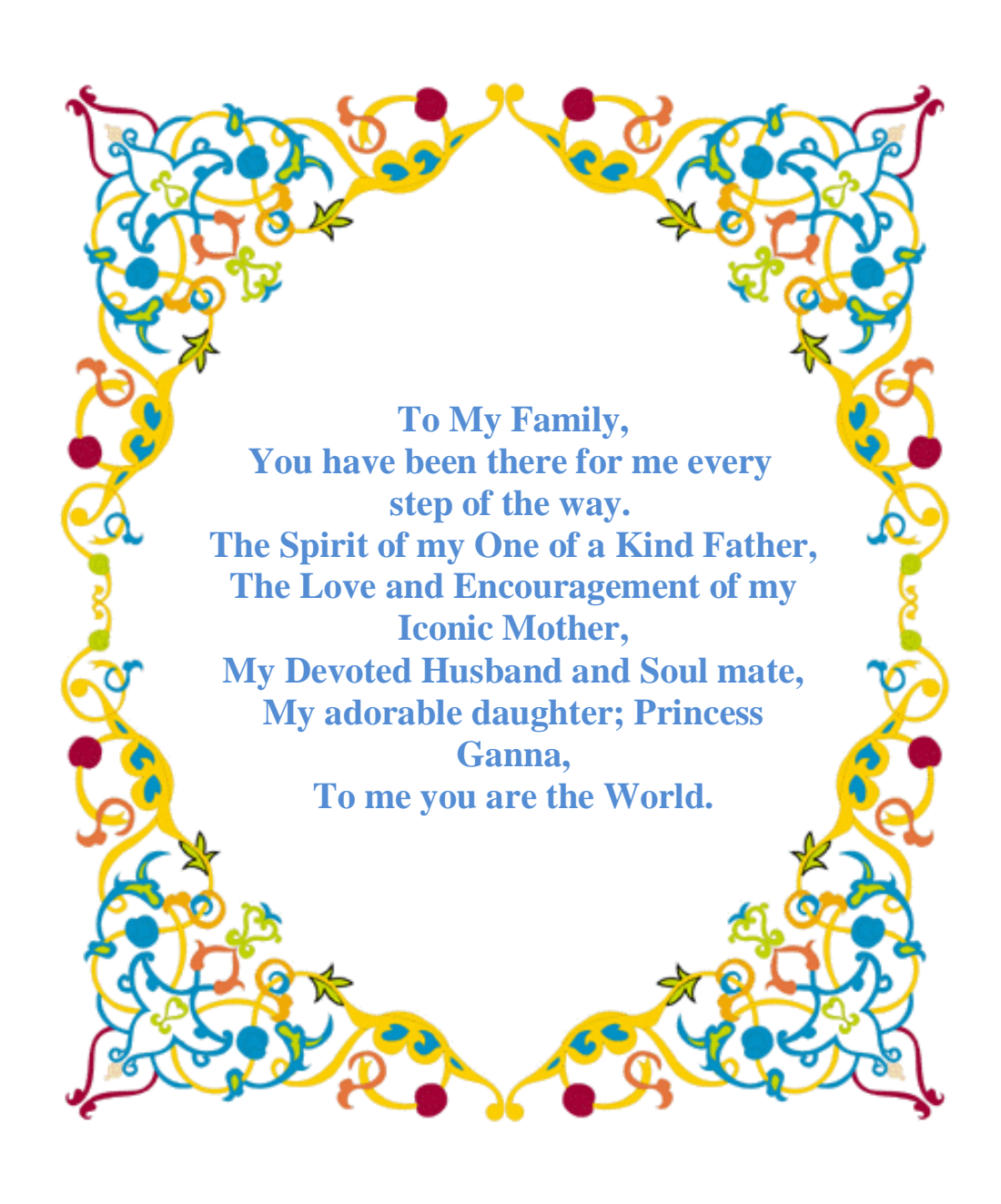


First of all, great thanks to **Allah** who enabled us to complete this work, hoping to provide a useful guide in the track of management of cancer patients.

No words can express my deepest appreciation and profound respect to **Prof. Dr. Hala Mahmoud Abou Senna,** Professor of Radio diagnosis, Ain Shams University, for her continuous guidance, support and constructive criticism throughout the work. She has generously devoted much of her time and effort. It was a great honor working under her supervision.

Also, my gratitude goes to **Prof. Dr. Annie Mahmoud Nasr Mehana,** Professor of Radio diagnosis, Ain Shams
University, for her guidance and support.





## **Contents**

Title	Page	
List of Abbreviation		I
List of Figures		III
List of Tables		XIV
Introduction and Aim of the Work	•••••	1
Review of Literature:		
Chapter (1): Epidemiology and Pathology of B	Breast and	
Lung Cancer		5
Chapter (2): An Outlook on the Pathogenesis	of Bone	
Metastases		38
Chapter (3): Imaging in Bone Metastases	•••••	44
Chapter (4): Physical Principals of DWI a	and ADC	
Mapping		89
Chapter (5): Technical Considerations		110
Patients and Methods		119
Results	•••••	128
Illustrated Cases	•••••	176
Discussion		229
Summary and Conclusion		261
Recommendations		267
References		268
Arahic Summary		

## **List of Abbreviations**

Abb.	Meaning
AC	Adenocarcinoma.
ADC	Apparent Diffusion Coeffecient.
AJCC	American Joint Committee of Cancer.
ASII	Adrenal Signal Intensity Index.
ASR	Active Search Results.
ASR	Adrenal-to-spleen chemical shift ratio.
AUC	Area under the Curve.
<b>BRCA 1,2</b>	Breast Cancer types 1, 2 Susceptibility Protein.
BV	Blood Volume.
CNR	Contrast to Noise Ratio.
CT	Computed Tomography.
CTH	Chemotherapy.
DCE-MRI	Dynamic Contrast Enhanced- Magnetic
	Resonance Imaging.
DCIS	Ductal Carcinoma In Situ.
DTC's	Disseminated Tumor Cells.
DWI	Diffusion Weighted Imaging.
DWIBS	Diffusion Weighted Imaging with Background
	Body Signal Suppression.
ECM	Extracellular Matrix.
EGFR	Epidermal Growth Factor Receptor.
EPI	Echo Planar Imaging.
FDG	Fluoro Deoxy Glucose.
FNAC	Fine Needle Aspiration and Cytology.
HER2	Human Epidermal Growth Factor receptor 2.
K <sub>ep</sub>	Reflux Constant.
K <sup>trans</sup>	Vascular Transfer Constant.
LCIS	Lobular Carcinoma In Situ.
MBq	MegaBecquerels.
mCi	Millicurie
MDA	M.D. Anderson Cancer Center.
MDP	Methylene Diphosphonate.
MIP	Maximum Intensity Projection.
MPG	Motion Probing Gradient.

Abb.	Meaning
MPR	Multi Planar Reconstruction.
NOPR	National Oncologic PET Registry
NPI	Nottingham Prognostic Index.
NPV	Negative Predictive Value.
NSCLC	Non Small Cell Lung Cancer.
P53	Tumor Protein 53.
PET	Positron Emission Tomography.
PPV	Positive Predictive Value.
PTEN	Phosphatase and Tensin Homolog.
RF	Radiofrequency.
ROC	Receiver Operating Characteristics.
ROI	Region of Interest.
RTH	Radiotherapy.
Scc	Short for Sarcoma (Proto-Oncogene tyrosine
	protein kinase enzyme)
SCC	Squamous Cell Carcinoma.
SCLC	Small Cell Lung Cancer.
SIADH	Syndrome of Inappropriate Antidiuretic Hormone
	secretion.
SM	Sunitinib Malate.
SNR	Signal to Noise Ratio.
SPECT	Single Photon Emission Computed Tomography.
STIR	Short Tau Inversion Recovery.
STK11	Serine/Threonine Kinase 11.
SUV	Standard Uptake Value.
SUVmax	Maximum Standard Uptake Value.
TE	Echo Time.
TIM	Total Imaging Matrix.
TR	Repetition Time.
USPIO's	Ultra Small Particles of Iron Oxide.
VDI	Vessel Density Index.
VSI	Vessel Size Imaging.
WB-MRI	Whole Body- Magnetic Resonance Imaging.
WHO	World Health Organization.
ZA	Zoledronic Acid.

## **List of Figures**

Figure	Title	Page
Fig. (1)	Bar chart representing incidence and	5
	mortality rates of different malignancies in	
	the female population according to WHO	
	statistics 2011.	
<b>Fig.</b> (2)	Diagram showing the normal balance	9
	between cell division and apoptosis opposed	
	to the uncontrolled cell division and failure of	
	apoptosis in malignancy.	
<b>Fig.</b> (3)	Pie chart showing the distribution of breast	16
	cancer subtypes.	
<b>Fig.</b> (4)	Histopathological slide of a well	17
	differentiated invasive ductal carcinoma.	
<b>Fig.</b> (5)	Histopathological slide of a moderately	17
	differentiated invasive ductal carcinoma.	
<b>Fig.</b> (6)	Histopathological slide of a high grade	18
	invasive ductal carcinoma.	
<b>Fig.</b> (7)	Diagram representing T staging of breast	20
	malignancy.	
<b>Fig.</b> (8)	Flow chart summarizing the different	23
	categories of breast malignancies based on	
	receptor presentations.	
<b>Fig.</b> (9)	Cancer progresses through aberrant cell	24
	differentiation due to alterations in gene	
	expression.	
<b>Fig.</b> (10)	Bar chart representing incidence and	26
	mortality rates of different malignancies in	
	both male and female populations according	
E:~ (11)	to WHO statistics 2011.	20
<b>Fig.</b> (11)	Oncogenesis theory based on inactivation of	29
E:~ (12)	tumor suppressor genes.	20
<b>Fig.</b> (12)	Oncogenesis theory based on activation of	30
E:- (12)	oncogenes.	22
Fig. (13)	Microscopic appearance of the different	32
	histopathological categories of lung cancer.	

Figure	Title	Page
Fig. (14)	Diagram showing the predilection of SCC and SCLC for central involvement and peripheral involvement in case of AC and NSCLC.	32
Fig. (15)	Common sites of metastases in various primaries.	38
Fig. (16)	Diagram illustrating the route of cancer cells initiating abnormal bone deposition (sclerotic lesions) and bone resorption (lytic lesions).	40
Fig. (17)	Illustrative diagram showing steps of vascular dissemination and metastatic spread.	41
Fig. (18)	Illustrative diagram specific for osseous metastases following vascular dissemination of cancer cells.	41
Fig. (19)	A model for the survival and emergence of latent disseminated tumor cells (DTCs) in the bone marrow.	43
Fig. (20)	Lateral radiograph shows mixed osteolytic-sclerotic bone metastases in the skull vault.	44
Fig. (21)	AP Radiograph of the knee shows osteolytic metastasis in the distal femur of a 51-year-old woman with breast carcinoma.	45
Fig. (22)	Lateral radiograph of the lumbar spine shows sclerotic metastasis of L2 vertebra in a 54-year-old man with lung cancer.	46
Fig. (23)	Axial computed tomography scan shows 2 rounded, mixed osteolytic-sclerotic lesions in a thoracic vertebral body.	47
Fig. (24)	CT-guided biopsy performed in the left ilium of a 50-year-old woman with an unknown primary tumor.	48
Fig. (25)	Axial computed tomography scan shows a destructive osteolytic lesion in the left acetabulum of a woman with breast cancer.	49
Fig. (26)	A normal bone scan in a 7 – year- old boy showing hot uptake at the growth plates.	51

Figure	Title	Page
Fig. (27)	A normal bone scan in a 43 – year- old	52
	woman.	
<b>Fig.</b> (28)	A case of metastatic bone disease showing	53
	multiple randomly distributed hot spots	
	implicating both axial and appendicular	
71 (20)	skeleton.	
Fig. (29)	A case of thyroid cancer with left iliac bone	54
	osteolytic metastasis showing an incomplete	
E: (20)	reactive osteoblastic rim.	
Fig. (30)	A metastatic superscan in a case of breast	56
Fig. (21)	cancer with extensive osseous involvement.  A case of breast cancer with diffuse	57
Fig. (31)	A case of breast cancer with diffuse considerable hot uptake along scanned	37
	vertebrae together with the abnormal uptake	
	at right hypochondrial region.	
Fig. (32)	Left anterior view of the chest from a 99m	58
119. (32)	Tc-MDP bone scan of patient with left-breast	30
	cancer showing abnormal soft-tissue uptake	
	in the region of the left breast	
Fig. (33)	Scintigraphic flare	59
Fig. (34)	FDG-PET CT examination demonstrates	63
	innumerable areas of bony metastatic disease	
	seen throughout the spine, the pelvis, bilateral	
	ribs and the proximal appendicular skeleton	
	bilaterally.	
Fig. (35)	A -50 year old- male patient with metastatic	64
	lung cancer with multiple osseous metastatic	
	deposits showing avid FDG uptake.	
Fig. (36)	Diagrammatic demonstration of skeletal	65
	uptake of sodium fluoride.	
Fig. (37)	MIP images of anteroposterior and left lateral	66
	views of a normal fluoride PET scan.	
Fig. (38)	Superscan pattern of a fluoride PET scan in	66
	metastatic prostate cancer.	

Figure	Title	Page
Fig. (39)	An 82-y-old patient with numerous bone metastases on anterior planar BS, multi-FOV SPECT, and <sup>18</sup> F-Fluoride PET images.	67
<b>Fig.</b> (40)	Bull's eye sign on T1W image.	69
Fig. (41)	Another example of Bull's eye sign.	70
Fig. (42)	Halo sign on STIR sequence.	71
Fig. (43)	A 69-year-old man with lytic and sclerotic metastases from prostate cancer.	71
Fig. (44)	Time interval changes in a 72- year- old male patient with right hip pain.	72
Fig. (45)	T1W and Diffusion MRI of the bone marrow in an 80-year-old man with hormone refractory metastatic prostate cancer.	74
Fig. (46)	MR features of a right iliac bone metastatic lesion.	75
Fig. (47)	A male patient with renal cancer complaining of back pain.	76
Fig. (48)	Whole-body MRI, including DWI, in a 66-year-old patient with prostate cancer and bone metastases.	77
Fig. (49a)	Inverted-gray-scale whole-body DW MR images obtained before therapy and after 7 months of treatment.	79
Fig. (49b)	ADC maps and histogram analysis in the follow up of the same patient.	80
Fig. (50)	A known case of cancer prostate showing significant progression in osseous metastatic load.	81
Fig. (51)	Schematic representations of the biological processes associated with changes in tumor ADC values with treatment.	83
Fig. (52)	Color maps of bone metastases as imaged by DCE-MRI and VSI (Vessel Size Imaging) at days 0, 5, and 25 to therapy.	85

Figure	Title	Page
Fig. (53)	Diagram showing capabilities of the different imaging modalities in the assessment of bone lesions based on their distribution.	88
Fig. (54)	Stejskal and Tanner adopted T2-weighted spin-echo sequence for measuring water diffusion.	90
Fig. (55)	Diagram illustrates the effect of a diffusion- weighted sequence on water molecules within highly cellular tissues or a restricted environment.	91
Fig. (56)	Diagram illustrates the effect of a diffusion-weighted sequence on water molecules within tissues with low cellularity or a less restricted environment.	92
Fig. (57)	A comparative diagram between free diffusivity and impeded diffusivity.	93
Fig. (58)	A graph representing the progressive loss of signal on DWI's in tissues with restricted diffusivity being smaller than for normal diffusivity on increasing b-values.	96
Fig. (59)	Effect of raising the b value on the characterization of lesions.	97
Fig. (60)	T2 shine-through effect.	98
Fig. (61)	A graph representing the progressive loss of signal on DWI's in benign lesions, malignant lesions and T2 shine-through, on increasing b-values.	99
Fig. (62)	Diffusion behaviour in a haemangioma.	101
Fig. (63)	The various ways of assessing ADC values.	104
Fig. (64)	The concept of DWIBS being insensitive to motion artifacts.	106
Fig. (65)	Coronal maximum intensity projection DWIBS images (inverted grey scale) of healthy volunteers	107

Figure	Title	Page
Fig. (66)	The volumetric nature of DWIBS facilitates	107
	reliably diagnostic MPR's in different planes.	
Fig. (67)	A 78-year-old man with metastatic and	108
	benign lesions visualized through DWIBS.	
<b>Fig.</b> (68)	Whole-body MRI. The patient is moved	110
	through a minimum of four different stations	
F: ((0))	to image the entire body.	114
<b>Fig.</b> (69)	Diagram shows the Total Imaging Matrix	114
Fig. (70)	multichannel surface coil system.	115
Fig. (70)	Automatic table movement at different anatomical regions at whole-body MRI	113
	examination.	
Fig. (71)	Pie chart representing regions targeted for	131
118 (71)	biopsy and histopathological verification their	101
	lesions.	
Fig. (72)	Graph showing an abundance of vertebral	132
	lesions detected on bone scan followed by	
	pelvic, and then thoracic, appendicular and	
	last are the calvarial lesions.	
<b>Fig.</b> (73)	Graph showing regional distribution of	133
	confidently diagnosed osseous metastatic	
	lesions out of the total number of detected lesions on bone scan.	
Fig. (74)	Pie chart displaying the distribution of the 19	135
Fig. (74)	false positive lesions on Bone Scan.	133
Fig. (75)	Chart displaying the fates of the lesions that	136
118 (70)	were reported metastatic or benign and those	100
	considered equivocal.	
Fig. (76)	Chart showing how the 60 patients were	137
	categorized based on bone scan findings after	
	verification of their lesions through biopsy or	
	follow up.	
Fig. (77)	Chart displaying the distribution of the 15	139
	false negative lesions on bone scan.	
Fig. (78)	Graph showing an abundance of vertebral	140

Figure	Title	Page
	lesions detected on WB-MRI without diffusion followed by pelvic, appendicular then thoracic and the last are the calvarial lesions.	
Fig. (79)	Graph showing regional distribution of lesions detected on WB-MRI with diffusion showing similar prevelance of vertebral lesions yet with more lesions detected in all regions sparing calvarial lesions.	141
Fig. (80)	Graph comparing the capability of each modality in the regional detection of lesions (both benign & malignant).	142
Fig. (81)	Graph comparing the capability of each modality in confidently reporting metastatic lesions.	142
Fig. (82)	Diagram showing the distribution of lesions detected on DWI.	146
Fig. (83)	Pie chart demonstrating the fate of lesions only seen DWI's and not on conventional MR images.	147
Fig. (84)	Chart displaying the fate of the lesions that were reported metastatic or benign and those considered equivocal.	149
Fig. (85)	Chart showing how the 60 patients were categorized based on WB-MRI findings without diffusion after verification of their lesions through biopsy or follow up.	150
Fig. (86)	Chart displaying the fate of the lesions that were reported metastatic or benign and those considered equivocal.	152
Fig. (87)	Chart showing how the 60 patients were categorized based on bone scan findings after verification of their lesions through biopsy or follow up.	152
Fig. (88)	Graph comparing the number of true positive,	155

Figure	Title	Page
	false positive, true negative and false negative lesions on bone scan, WB-MRI with and without diffusion.	
Fig. (89)	ROC curves for the four-point scale predictive variables between whole-body MRI and bone scintigraphy.	159
Fig. (90)	Diffusion-weighted imaging revealed significantly higher CNR than did STIR and T1-weighted SE sequences.	161
Fig. (91)	Showing the overlap in ADC values between different pathological entities.	163
Fig. (92)	Diagram showing the soft tissue metastatic involvement (true positive) detected on WB-MRI without diffusion.	168
Fig. (93)	Diagram showing the soft tissue metastatic involvement (true positive) detected on WB-MRI with diffusion.	172
Fig. (94)	Case 1: A 45-year-old female patient with recently diagnosed breast cancer.	177
Fig. (95)	Case 1: A 45-year-old female patient with recently diagnosed breast cancer.	178
Fig. (96)	Case 2: A 51-year-old female patient with breast cancer that was subjected to MRM and received CTH and RTH.	181
Fig. (97)	Case 2: A 51-year-old female patient with breast cancer that was subjected to MRM and received CTH and RTH.	182
Fig. (98)	Case 2: A 51-year-old female patient with breast cancer that was subjected to MRM and received CTH and RTH.	183
Fig. (99)	Case 3: A 58-year-old female patient with lung cancer who had been on CTH.	186
Fig. (100)	Case 3: A 58-year-old female patient with lung cancer who had been on CTH.	187
Fig. (101)	Case 3: A 58-year-old female patient with	188

Figure	Title	Page
	lung cancer who had been on CTH.	
Fig. (102)	Case 4: A 38-year-old female patient with metastatic right breast cancer to the liver and bones.	191
Fig. (103)	Case 4: A 38-year-old female patient with metastatic right breast cancer to the liver and bones.	192
Fig. (104)	Case 4: A 38-year-old female patient with metastatic right breast cancer to the liver and bones.	193
Fig. (105)	Case 4: A 38-year-old female patient with metastatic right breast cancer to the liver and bones.	194
Fig. (106)	Case 5: A 51-year-old male patient with recurrent left lung cancer for which patient was subjected to surgical resection and CTH.	196
Fig. (107)	Case 5: A 51-year-old male patient with recurrent left lung cancer for which patient was subjected to surgical resection and CTH.	197
Fig. (108)	Case 5: A 51-year-old male patient with recurrent left lung cancer for which patient was subjected to surgical resection and CTH.	198
Fig. (109)	Case 5: A 51-year-old male patient with recurrent left lung cancer for which patient was subjected to surgical resection and CTH.	198
Fig. (110)	Case 6: A 58-year-old male patient with left lung cancer for which he received CTH and RTH.	201
Fig. (111)	Case 6: A 58-year-old male patient with left lung cancer for which he received CTH and RTH.	202
Fig. (112)	Case 6: A 58-year-old male patient with left lung cancer for which he received CTH and RTH.	203
<b>Fig.</b> (113)	Case 7: A 52-year-old male patient with left	205